JOURNAL OF COMPUTATIONAL PHYSICS 105, 47–57 (1993)

Computing the Flow around a Submerged Body Using Composite Grids

N. ANDERS PETERSSON AND JOHAN F. MALMLIDEN

Center for Computational Mathematics and Mechanics, Royal Institute of Technology, S-100 44 Stockholm, Sweden

Received January 28, 1991; revised May 28, 1992

The subject of this paper is an accurate numerical method for solving the linear two-dimensional steady potential flow around a body which moves in a liquid of finite constant depth at constant speed and distance below the free surface. The differential equation is discretized by a second-order accurate finite difference scheme on a composite grid. The composite grid consists of two overlapping component grids; one curvilinear grid close to the body and one Cartesian grid which covers the surrounding liquid. To solve the problem numerically, the infinite domain is truncated to finite length. The inflow and outflow boundary conditions are formed by making an eigenfunction expansion of the solution ahead of and behind the body. Each eigenfunction is required to be bounded and satisfy the upstream condition at infinity. This is imposed by functional relations between the solution and its normal derivative at the inflow and outflow boundaries. The method is carefully validated and the computed solutions are found to be in very good agreement with existing results.

1. INTRODUCTION

Consider the two-dimensional steady potential flow around a submerged body moving in a liquid of finite constant depth at constant speed and distance below the free surface. The physical quantities are scaled by the speed of the body, U, and the length of the gravity waves behind it, U^2/g, where g is the acceleration of gravity. The motion is described in Cartesian coordinates fixed with respect to the body, where the x-axis points opposite to the forward velocity and the z-axis is directed vertically upwards. $z=-d$ corresponds to the bottom and $z=0$ to the undisturbed free surface, where d is the non-dimensional depth. The total velocity potential is split into a free stream potential plus a perturbation potential: $\Phi = x + \phi$. By linearizing the boundary condition at the free surface around the free stream flow, cf. [12], the following problem is obtained for the perturbation potential:

$$\Delta\phi = 0, \quad -\infty < x < \infty, -d < z < 0, \tag{1}$$

together with the boundary conditions,

$$\phi_{xx} + \phi_z = 0 \quad -\infty < x < \infty, z = 0 \tag{2}$$

$$\phi_z = 0 \quad -\infty < x < \infty, z = -d \tag{3}$$

$$\partial\phi/\partial n + \cos\theta = 0 \quad \text{on the body.} \tag{4}$$

Here $\partial/\partial n$ denotes the outward normal derivative and θ is the angle between the outwardly directed normal to the body and the x-direction. The steady solution is regarded as the large-time limit of an unsteady solution, where the body accelerates from rest to the constant velocity. This implies that the perturbation potential must tend to a constant value at large distances in front of the body. This condition will be called the upstream condition,

$$\lim_{x \to -\infty} \phi(x, z) = \text{const}, \quad -d < z < 0. \tag{5}$$

The aim of the research described here is to take a first step towards an accurate numerical method for the nonlinear potential problem, where the boundary condition at the free surface is not linearized. In particular, the method developed in this paper does not rely on the addition of artificial damping in the boundary condition at the free surface. Furthermore, the present method is possible to extend to incorporate effects of vorticity and viscosity.

Two main classes of numerical techniques have been used previously to solve the present problem. These are based on boundary integral methods and finite element techniques. There are two different types of boundary integral methods. The first uses a kernel which satisfies the boundary condition on the free surface and the upstream condition, cf. [4]. In this method, there are dependent variables only along the surface of the body but the kernel is rather difficult and expensive to evaluate numerically. Moreover, this technique is not generalizable to the nonlinear problem. The second boundary integral method employs a kernel which does not satisfy any boundary conditions but is easy and inexpensive to evaluate, cf. [3, 6]. The dependent variables are located along the boundary of the body and at the infinite surface, which needs to be truncated in the numerical approximation. This method has also been attempted for the nonlinear problem, cf. [7]. Here it is necessary to add artificial dissipation to the boundary condition at the free surface to obtain a solution which satisfies the boundary condition. To

581/105/1-4

0021-9991/93 $5.00

make the method work, it was found necessary to increase the artificial dissipation as the speed of the body was increased. However, it is not well understood how the dissipation affects the solution.

The finite element techniques are based on dividing the fluid domain into two subdomains, one close to the body and one outer domain. The domain close to the body is discretized by finite elements and analytical solutions are used ahead of and behind the body. This approach, called the hybrid element method, is pursued in [9]. In this method, the problem is split into a radiation and a diffraction problem. In two dimensions, it is necessary to solve one radiation problem and one diffraction problem. In three dimensions, one radiation problem still needs to be solved but it is now necessary to solve $O(N)$ diffraction problems if the domain is discretized by N elements sideways to the direction of motion.

Both the hybrid element method and the present technique have the potential of handling more realistic flow models, like the Euler or the Navier–Stokes equations. A more careful comparison between the two approaches is therefore appropriate. The present method is similar to the hybrid element method in that analytical solutions are used ahead of and behind the body. In both methods, the basic idea is to use these solutions to form functional relations which are satisfied by every bounded solution that fulfills the upstream condition. The functional relations are used as inflow and outflow boundary conditions for the problem close to the body. The major advantage of these boundary conditions is that they do not affect the solution close to the body at all. The principal difference between the inflow and outflow conditions in [9] and those in the present work lies in the treatment of the oscillatory component in the solution ahead of and behind the body. We exemplify the difference for the two-dimensional case where only one oscillatory component is present. In the hybrid element method, one relation is imposed at the inflow and one at the outflow boundary. The upstream condition requires both the oscillatory component and its horizontal derivative to vanish ahead of the body. In order to satisfy this, it is necessary to solve two linear problems with the same matrix but with different right-hand sides (the radiation and the diffraction problem). The linear combination of the two solutions that satisfies the upstream condition constitute the solution of the problem in question. In the present method, both conditions on the oscillatory component are imposed explicitly at the inflow boundary and no conditions at the outflow boundary. It is therefore possible to obtain a solution that satisfies the upstream condition by only solving one problem.

In the present work, we develop this idea to the discrete case when the problem is discretized by finite differences on a Cartesian grid. In this case, the boundary conditions are matrix relations between the dependent variables close to the boundary in question. To be able to handle bodies of general shape, a boundary-fitted curvilinear grid is used to cover the domain close to the body. This makes the discretization of the Neumann boundary condition on the body accurate and straightforward. The surrounding liquid is most easily covered with a Cartesian grid. The need for both a Cartesian grid and a curvilinear grid is satisfied by utilizing a composite overlapping grid, cf. [2].

For many realistic applications, the depth of the liquid is large. If a grid with constant vertical grid size is used to cover the surrounding liquid, the majority of grid points will be in the domain between the body and the bottom, where the solution can be expected to vary slowly. The most straightforward way to make our method efficient for this case is to stretch the grid in the vertical direction, so that the vertical grid size increases towards the bottom. Even more grid points would be saved if a coarse component grid is used to discretize the domain close to the bottom. However, these straightforward extensions of the method will not be addressed in the present paper.

The hybrid element method and the present method are similar in that they both discretize the flowfield. Both methods therefore use discrete approximations of the differential equation and the boundary conditions. If the same order of accuracy is employed in both approaches, it is to be expected that both methods would produce similar results on grids of comparable resolution. If a direct method, like Gaussian elimination, is used to solve the occurring linear systems of equations, the hybrid element formulation in [9] has the advantage that the system matrix is symmetric. It is slightly faster and less memory consuming to solve such a problem than the unsymmetric linear system that emanates from the present method. Only the comparison between practical implementations of both methods could elucidate whether it is faster to solve one unsymmetric linear problem compared to two symmetric ones.

The linear systems become too large to be solved by a direct method in the three-dimensional case, so both the hybrid element and the present method must utilize iterative techniques. An efficient iterative scheme for the present method has recently been developed, cf. [8], and we are presently implementing it for the three-dimensional case. At this time, it is therefore difficult to predict the relative performance of the two methods. However, one advantage of the present method is that it only requires the solution of one problem, cf. [10], in contrast to the $\mathcal{O}(N)$ problems in the hybrid element method. It is the belief of the authors that the present method will prove to be superior in the three-dimensional case.

2. THE COMPOSITE GRID

The composite grid method is a general tool for solving PDEs on complex domains, cf. [2]. The basic idea is to

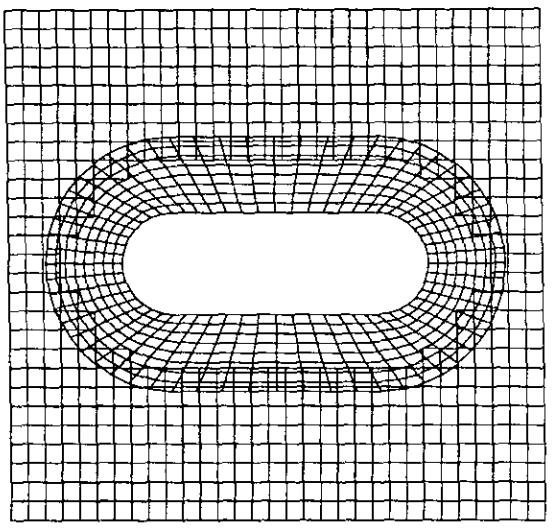

FIG. 1. A composite grid.

divide the complex domain into simple overlapping subdomains, the union of which completely covers the region of interest. Each subdomain is covered by a component grid. This set of component grids taken together is called a composite grid. The component grids overlap each other with no requirement that they exactly match up at their edges. The main advantage compared to covering the whole domain with one single grid is that each component grid can be chosen to have a smooth transformation to the unit square; in particular it can be made without singularities. An example of a composite grid is given in Fig. 1.

Each component grid can be constructed almost independently of the other components grids. However, one constraint is that the overlap must be sufficiently large so that accurate interpolation relations can be formed. To minimize the number of grid points it is also desirable that the grid spacing be about the same on each grid where two component grids overlap.

The grid-generation program CMPGRD, cf. [1], was employed to construct the composite grids. This program supplies all the information needed to form the difference equations and the interpolation relations. Furthermore, CMPGRD is capable of constructing three-dimensional composite grids, so the present method can be extended to three dimensions.

3. THE COMPONENT GRIDS

In the present case, the composite grid consists of two overlapping component grids. The domain close to the body, Ω_B, is covered by the curvilinear grid G_B and the surrounding sea, Ω_C, is covered by the Cartesian grid G_C, cf. Fig. 2 and Fig. 3. Each component grid is bounded by four smooth boundary curves. For the grid G_C, these are the free

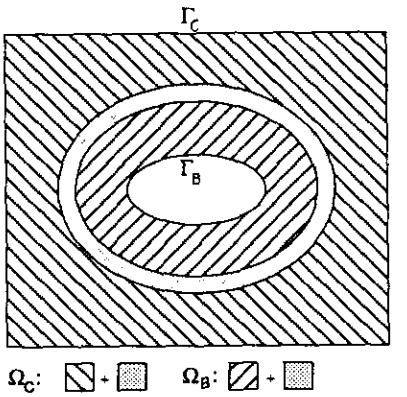

FIG. 2. The two subdomains.

surface, the bottom, and the inflow and outflow boundaries. The grid G_B is wrapped around the body. In this case the boundary curves consists of the body surface, the outer boundary, and the periodic boundary. The outer boundary is located at an approximately constant distance from the body and the periodic boundary is situated between the rightmost points on the body boundary and the outer boundary.

We define the grid points in the Cartesian grid G_C by

$$x_k = a + (k-1)\,h_x, \qquad k = 0, 1, \ldots, N^C + 1 \tag{6}$$

$$z_j = -d + (j-1)\,h_z, \qquad j = 1, 2, \ldots, M^C, \tag{7}$$

where the constants a and b are chosen such that the domain Ω_B is contained within $a < x < b$. The grid sizes are $h_z = d/(M^C - 1)$ and $h_x = (b-a)/(N^C - 1)$, where $M^C > 1$ and $N^C > 1$ are natural numbers.

The curvilinear grid G_B can be viewed as the discrete image of a mapping from a unit square in the (r, s) plane onto Ω_B. The mapping can formally be written as

$$\begin{aligned} x &= x^B(r, s) \\ z &= z^B(r, s) \end{aligned} \tag{8}$$

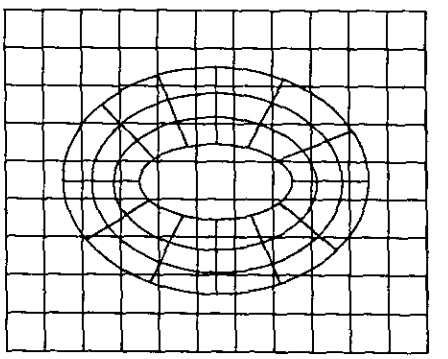

FIG. 3. The two component grids.

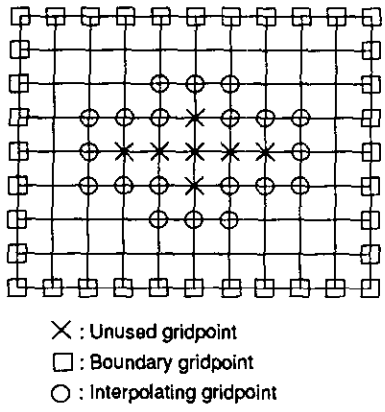

FIG. 4. Different types of grid points in the grid G_C.

and the grid points are given by $x_{k,j} = x^B(r_k, s_j)$ and $z_{k,j} = z^B(r_k, s_j)$, where

$$r_k = (k-1)\,h_r, \quad k = 1, 2, ..., N^B \tag{9}$$

$$s_j = (j-1)\,h_s, \quad j = 1, 2, ..., M^B. \tag{10}$$

The grid sizes are $h_r = 1/(N^B - 1)$ and $h_s = 1/(M^B - 1)$, where $M^B > 1$ and $N^B > 1$ are natural numbers. To obtain a useful grid, the mapping $(r, s) \to (x^B, z^B)$ is required to be smooth, one to one, and onto Ω_B. The mapping is constructed such that constant-s lines wrap around the body with r increasing clockwise. Constant-r lines go from the body surface to the outer surface, with s increasing outwards. This implies that (r, s) is positively oriented. Furthermore, the grid is periodic in the r-direction with $x_{i,j} \equiv x_{i+N^B-1,j}$ and $z_{i,j} \equiv z_{i+N^B-1,j}$ for $j = 1, 2, ..., M^B$. The grid line r_{N^B} will not be used in the following.

In practice, the mapping functions x^B and z^B are often only known at the grid points. However, as we will see below, this information is sufficient to form the difference scheme, provided the underlying mapping functions are smooth.

To better resolve the details in the solution close to the body surface, we give the grid G_B higher priority than the grid G_C. This means that all grid points of grid G_B will be used in the discretization of the problem, while some grid points of grid G_C in the region of overlap will not be used. The algorithm that decides which gridpoints will be used and how they will be used is the backbone of the program CMPGRD. It is thoroughly described in [2]. In the following, let $(j, k) \in I_C$ denote the set of indices of used grid points (x_j, z_k) in the grid G_C which are not located at the boundary and not neighbor to an unused grid point, cf. Fig. 4.

4. DISCRETIZING THE EQUATIONS

We define a grid function on grid G_C by $f_{j,k} = f(x_j, z_k)$ and on grid G_B by $g_{j,k} = g(x^B(r_j, s_k), z^B(r_j, s_k))$. The forward and backward divided difference operators in the x-direction on the grid G_C are defined as

$$D_+^x f_{j,k} = \frac{f_{j+1,k} - f_{j,k}}{h_x} \tag{11}$$

$$D_-^x f_{j,k} = \frac{f_{j,k} - f_{j-1,k}}{h_x}. \tag{12}$$

The corresponding operators in the z-direction on the grid G_C and in the r- and s-directions on the grid G_B are defined in a similar way. We also define the central divided difference operator as

$$D_0 = \tfrac{1}{2}(D_+ + D_-). \tag{13}$$

On the Cartesian grid, G_C, we directly discretize the Laplace equation by second-order accurate central differences. This yields

$$\Delta\phi(x_j, z_k) = (D_+^x D_-^x + D_+^z D_-^z)\,\phi_{j,k} + \mathcal{O}(h_x^2) + \mathcal{O}(h_z^2) \tag{14}$$

for $(j, k) \in I_C$.

To discretize the Laplace equation on the curvilinear grid, G_B, it is first transformed to the (r, s) plane by Eq. (8). This gives the following second-order PDE with variable coefficients:

$$A(r,s)\frac{\partial\phi}{\partial r} + B(r,s)\frac{\partial\phi}{\partial s} + C(r,s)\frac{\partial^2\phi}{\partial r^2} + D(r,s)\frac{\partial^2\phi}{\partial s^2} + E(r,s)\frac{\partial^2\phi}{\partial r\,\partial s} = 0. \tag{15}$$

The coefficients are given by, cf. [11],

$$\begin{aligned} A(r,s) = (&-x_{rr}z_s^3 + 2x_{rs}z_r z_s^2 + x_s z_{rr} z_s^2 \\ &- 2x_s z_r z_{rs} z_s - x_{ss} z_r^2 z_s + x_s z_r^2 z_{ss} + 2x_r x_s x_{rs} z_s \\ &+ x_r^2 x_s z_{ss} - 2x_r x_s^2 z_{rs} - x_r^2 x_{ss} z_s \\ &- x_{rr} x_s^2 z_s + x_s^3 z_{rr})/(x_r z_s - x_s z_r)^3 \end{aligned} \tag{16}$$

$$\begin{aligned} B(r,s) = (&x_{ss} z_r^3 + 2x_r z_r z_{rs} z_s - x_r z_r^2 z_{ss} \\ &- 2x_{rs} z_r^2 z_s + x_{rr} z_r z_s^2 - x_r z_s^2 z_{rr} - 2x_r x_s x_{rs} z_r \\ &- x_r x_s^2 z_{rr} + 2x_r^2 x_s z_{rs} + x_r^2 x_{ss} z_r \\ &+ x_s^2 x_{rr} z_r - x_r^3 z_{ss})/(x_r z_s - x_s z_r)^3 \end{aligned} \tag{17}$$

$$C(r,s) = (x_s^2 + z_s^2)/(x_r z_s - x_s z_r)^2 \tag{18}$$

$$D(r,s) = (x_r^2 + z_r^2)/(x_r z_s - x_s z_r)^2 \tag{19}$$

$$E(r,s) = -2(x_r x_s + z_r z_s)/(x_r z_s - x_s z_r)^2. \tag{20}$$

Here, x_r, z_r, etc. denote differentiation of the grid transformations $x^B(r, s)$ and $z^B(r, s)$, respectively. The transformed

equation is discretized by central differences, which gives the nine-point formula

$$\Delta\phi(x^B(r_j, s_k), z^B(r_j, s_k)) = \sum_{p=-1}^{1} \sum_{q=-1}^{1} \gamma_{p,q}(j,k)\, \phi_{j+p,k+q} + \mathcal{O}(h_s^2) + \mathcal{O}(h_r^2) \tag{21}$$

for $2 \leqslant j \leqslant N^B - 2$ and $2 \leqslant k \leqslant M^B - 1$. The coefficients $\gamma_{p,q}(j,k)$ are given by

$$\gamma_{-1,-1} = \frac{E_{j,k}}{4h_r h_s}, \qquad \gamma_{0,-1} = -\frac{B_{j,k}}{2h_s} + \frac{D_{j,k}}{h_s^2},$$

$$\gamma_{1,-1} = -\frac{E_{j,k}}{4h_r h_s}, \qquad \gamma_{-1,0} = -\frac{A_{j,k}}{2h_r} + \frac{C_{j,k}}{h_r^2},$$

$$\gamma_{0,0} = -\frac{2C_{j,k}}{h_r^2} - \frac{2D_{j,k}}{h_s^2}, \qquad \gamma_{1,0} = \frac{A_{j,k}}{2h_r} + \frac{C_{j,k}}{h_r^2},$$

$$\gamma_{-1,1} = -\frac{E_{j,k}}{4h_r h_s}, \qquad \gamma_{0,1} = \frac{B_{j,k}}{2h_s} + \frac{D_{j,k}}{h_s^2},$$

$$\gamma_{1,1} = \frac{E_{j,k}}{4h_r h_s}.$$

Here $A_{j,k}, \ldots, E_{j,k}$ represent the functions $A(r_j, s_k), \ldots, E(r_j, s_k)$ discretized by second-order accurate central differences. We now have one equation for each interior grid point. To close the system, one equation is needed for each grid point on the boundaries.

5. THE INFLOW AND OUTFLOW BOUNDARY CONDITIONS

To solve the problem numerically, the infinite domain is truncated to $a \leqslant x \leqslant b$, where $b - a < \infty$. The solution is assumed to be bounded and satisfy the upstream condition Eq. (5) at infinity. These conditions are translated into functional relations between the value and the normal derivative of the solution at the inflow and outflow boundaries. These relations are derived by making an eigenfunction expansion of the solution in the z-direction ahead of and behind the body. To each eigenfunction is the z-direction there is a corresponding eigenfunction in the x-direction. The relations are found by requiring the x-eigenfunctions to have the proper behavior at infinity. They are imposed as boundary conditions at $x = a$ and $x = b$.

This approach is also possible in the discrete case, where the boundary conditions take the form of matrix relations between the value and the normal divided difference of the solution at the in and outflow boundaries.

Once the problem in $a \leqslant x \leqslant b$ has been solved, the solutions in $-\infty < x < a$ and $b < x < \infty$ can be constructed from the solution and its normal derivative at the boundaries $x = a$ and $x = b$, respectively.

5.1. *The Continuous Case*

To solve Eqs. (1)–(5) in $x \leqslant a$ and $x \geqslant b$ we use separation of variables, $\phi(x, z) = \mathcal{R}(x)\, \mathcal{S}(z)$. In the z-direction, this implies

$$\mathcal{S}'' - \lambda \mathcal{S} = 0, \quad -d \leqslant z \leqslant 0, \tag{22}$$

$$\mathcal{S}'' - \mathcal{S}' = 0, \quad z = 0, \tag{23}$$

$$\mathcal{S}' = 0, \quad z = -d. \tag{24}$$

This problem is not in self-adjoint form with respect to the $\mathcal{L}_2$ scalar product, i.e., $\langle f, g \rangle_2 = \int_{-d}^{0} \bar{f}(z)\, g(z)\, dz$. However, introducing $\zeta(z) = \mathcal{S}'(z)$ and differentiating Eq. (22) transforms the equation into a self-adjoint eigenvalue problem for ζ. The eigenvalues are the solutions of

$$\sqrt{\lambda} = \tanh \sqrt{\lambda}\, d. \tag{25}$$

If $d > 1$, there is one real eigenvalue $\sqrt{\lambda_1} > 0$; otherwise there are no nonzero real eigenvalues. Introducing $\sqrt{\lambda_k} = i\sqrt{\mu_k}$ yields an infinite number of eigenvalues $0 < \sqrt{\mu_2} < \sqrt{\mu_3} < \cdots$. The corresponding eigenfunctions can be written as

$$\zeta^{(1)}(z) = \sinh \sqrt{\lambda_1}\, (d + z) \tag{26}$$

$$\zeta^{(k)}(z) = \sin \sqrt{\mu_k}\, (d + z), \quad k = 2, 3, \ldots. \tag{27}$$

The eigenfunctions for $\mathcal{S}$ are found by integrating once. This gives

$$\mathcal{S}^{(0)}(z) = 1 \tag{28}$$

$$\mathcal{S}^{(1)}(z) = \cosh \sqrt{\lambda_1}\, (d + z) \tag{29}$$

$$\mathcal{S}^{(k)}(z) = \cos \sqrt{\mu_k}\, (d + z), \quad k = 2, 3, \ldots. \tag{30}$$

For convenience, the eigenfunctions have been normalized to exclude the factors $1/\sqrt{\lambda_1}$ and $1/\sqrt{\mu_k}$, respectively. The constant eigenfunction $\mathcal{S}^{(0)}$ corresponds to the eigenvalue $\sqrt{\lambda_0} = 0$. In the x-direction, Eq. (1) implies

$$\mathcal{R}^{(0)}(x) = A_0 + B_0 x \tag{31}$$

$$\mathcal{R}^{(1)}(x) = A_1 e^{i\sqrt{\lambda_1}\, x} + B_1 e^{-i\sqrt{\lambda_1}\, x} \tag{32}$$

$$\mathcal{R}^{(k)}(x) = A_k e^{-\sqrt{\mu_k}\, x} + B_k e^{\sqrt{\mu_k}\, x}, \quad k = 2, 3, \ldots. \tag{33}$$

Hence, the solution will only be oscillatory in the x-direction if $d > 1$. To summarize, the solution can be written as

$$\phi(x, z) = \sum_{k=0}^{\infty} \mathcal{R}^{(k)}(x)\, \mathcal{S}^{(k)}(z). \tag{34}$$

The orthogonality of the transformed eigenfunctions is used to determine $\mathscr{R}^{(k)}$, $k \geqslant 1$,

$$\mathscr{R}^{(k)}(x) = \frac{\langle \phi_z(x, \cdot), \mathscr{S}_z^{(k)} \rangle_2}{\|\mathscr{S}_z^{(k)}\|_2^2}, \quad k = 1, 2, \ldots, \tag{35}$$

where $\|f\|_2^2 = \langle f, f \rangle_2$. The function $\mathscr{R}^{(0)}$ cannot be determined in this way because $\mathscr{S}^{(0)}$ is annihilated by the transformation to self-adjoint form. Instead we use

$$\mathscr{R}^{(0)}(x) = \phi(x, z) - \sum_{k=1}^{\infty} \frac{\langle \phi_z(x, \cdot), \mathscr{S}_z^{(k)} \rangle_2}{\|\mathscr{S}_z^{(k)}\|_2^2} \mathscr{S}^{(k)}(z). \tag{36}$$

This equation is valid for $-d \leqslant z \leqslant 0$.

To obtain a bounded solution, we must impose restrictions on $\mathscr{R}^{(0)}$ and $\mathscr{R}^{(k)}$, $k \geqslant 2$. There must be no linearly growing modes ahead of or behind the body; $B_0 = 0$. Moreover, there can only be exponentially decaying modes; $A_k = 0$ ahead of the body and $B_k = 0$ behind it for $k \geqslant 2$.

We impose $B_0 = 0$ by differentiating Eq. (36) with respect to x and applying it to $z = -d$, i.e.,

$$\phi_x(x, -d) - \sum_{k=1}^{\infty} \frac{\langle \phi_{xz}(x, \cdot), \mathscr{S}_z^{(k)} \rangle_2}{\|\mathscr{S}_z^{(k)}\|_2^2} \mathscr{S}^{(k)}(-d) = 0. \tag{37}$$

The exponentially decaying modes satisfy $d\mathscr{R}^{(k)}/dx = \sqrt{\mu_k}\, \mathscr{R}^{(k)}$ ahead of the body and $d\mathscr{R}^{(k)}/dx = -\sqrt{\mu_k}\, \mathscr{R}^{(k)}$ behind it. Applying these relations to Eq. (35) yields

$$\langle \phi_{xz}(a, \cdot), \mathscr{S}_z^{(k)} \rangle_2 - \sqrt{\mu_k}\, \langle \phi_z(a, \cdot), \mathscr{S}_z^{(k)} \rangle_2 = 0 \tag{38}$$

$$\langle \phi_{xz}(b, \cdot), \mathscr{S}_z^{(k)} \rangle_2 + \sqrt{\mu_k}\, \langle \phi_z(b, \cdot), \mathscr{S}_z^{(k)} \rangle_2 = 0 \tag{39}$$

for $k \geqslant 2$.

The upstream condition, Eq. (5), implies that there must be no oscillatory component in the solution ahead of the body. This yields

$$\langle \phi_z(a, \cdot), \mathscr{S}_z^{(1)} \rangle_2 = 0 \tag{40}$$

$$\langle \phi_{xz}(a, \cdot), \mathscr{S}_z^{(1)} \rangle_2 = 0. \tag{41}$$

The oscillatory part of the solution behind the body depends on the solution close to the body.

We observe that a constant function is a solution of the homogeneous counterpart of Eqs. (1)–(5) and the in and outflow boundary conditions, Eqs. (37)–(41). To determine this constant and make the problem nonsingular, we enforce $\mathscr{R}^{(0)}(a) = 0$ instead of $B_0 = 0$ at $x = a$. This is done by applying Eq. (36) for $x = a$, $z = -d$. The value of B_0 cannot be enforced and will instead depend on the solution close to the body. However, as we will show in Section 5.2, it will always obtain the value zero.

5.2. *Boundedness of the Solution at $x = -\infty$*

To find the value of B_0 ahead of the body we integrate the differential equation over the domain $\Omega_B \cup \Omega_C$, $I = \int_{\Omega_B \cup \Omega_C} \Delta\phi \, dS = 0$. By integration by parts we obtain

$$I = \oint_{\Gamma_C} \frac{\partial \phi}{\partial n} d\Gamma - \oint_{\Gamma_B} \frac{\partial \phi}{\partial n} d\Gamma, \tag{42}$$

where $\partial/\partial n$ denotes the outward normal derivative. Inserting Eq. (4) yields that the contribution from the second integral is zero. By using the boundary conditions Eqs. (2), (3) the first integral can be written as

$$\oint_{\Gamma_C} \frac{\partial \phi}{\partial n} d\Gamma = \sigma(b) - \sigma(a), \tag{43}$$

where

$$\sigma(x) = \int_{-d}^{0} \frac{\partial \phi(x, \zeta)}{\partial x} d\zeta - \frac{\partial \phi(x, 0)}{\partial x}. \tag{44}$$

Inserting the eigenfunction expansion Eq. (34) yields

$$\sigma(x) = \sum_{k=0}^{\infty} \frac{d\mathscr{R}^{(k)}}{dx}(x) \left\{ \int_{-d}^{0} \mathscr{S}^{(k)}(\zeta)\, d\zeta - \mathscr{S}^{(k)}(0) \right\}. \tag{45}$$

By integrating Eqs. (28)–(30) and using the relation for the eigenvalues, Eq. (25), we find

$$\begin{aligned} &\int_{-d}^{0} \mathscr{S}^{(0)}(\zeta)\, d\zeta - \mathscr{S}^{(0)}(0) = d - 1 \\ &\int_{-d}^{0} \mathscr{S}^{(k)}(\zeta)\, d\zeta - \mathscr{S}^{(k)}(0) = 0, \quad k = 1, 2, 3, \ldots. \end{aligned} \tag{46}$$

Inserting these expressions into Eq. (45) gives

$$\sigma(x) = (d - 1) \frac{d\mathscr{R}^{(0)}}{dx}(x). \tag{47}$$

Behind the body, $B_0 = 0$, which implies $\sigma(b) = 0$. Therefore, $\sigma(a) = 0$ and $B_0 = 0$ ahead of the body as well.

5.3. *The Discrete Case*

A second-order accurate discretization of Eqs. (1)–(5) in $-\infty < x \leqslant a$ or $b \leqslant x < \infty$ is given by

$$(D_+^x D_-^x + D_+^z D_-^z)\, \phi_{k,j} = 0, \quad j = 1, 2, \ldots, M^C, \tag{48}$$

$$D_0^z \phi_{k,j} = 0, \quad j = 1, \tag{49}$$

$$(D_+^x D_-^x + D_0^z)\, \phi_{k,j} = 0, \quad j = M^C, \tag{50}$$

for $-\infty < k \leqslant 0$ or $N^C \leqslant k < \infty$, respectively. By separation of variables, cf. [10], the solution of Eqs. (48)–(50) may be expressed as

$$\phi_{k,j} = \sum_{p=0}^{M^C-1} \mathscr{G}_k^{(p)} \mathscr{H}_j^{(p)} \tag{51}$$

where

$$\mathscr{H}_j^{(0)} = 1 \tag{52}$$

$$\mathscr{H}_j^{(1)} = \cosh \sqrt{\kappa_1}\,(d + z_j) \tag{53}$$

$$\mathscr{H}_j^{(p)} = \cos \sqrt{\nu_p}\,(d + z_j), \quad p = 2, 3, \ldots, M^C - 1, \tag{54}$$

and

$$\mathscr{G}_k^{(0)} = A_0 + B_0 x_k \tag{55}$$

$$\mathscr{G}_k^{(1)} = A_1 e^{i\sqrt{\lambda_1}\,x_k} + B_1 e^{-i\sqrt{\lambda_1}\,x_k} \tag{56}$$

$$\mathscr{G}_k^{(p)} = A_p e^{-\sqrt{\mu_p}\,x_k} + B_p e^{\sqrt{\mu_p}\,x_k}, \quad p = 2, 3, \ldots, M^C - 1. \tag{57}$$

The eigenvalues in the z-direction are the solutions of

$$\frac{2}{h_z} \frac{\cosh(\sqrt{\kappa}\,h_z) - 1}{\sinh(\sqrt{\kappa}\,h_z)} = \tanh(\sqrt{\kappa}\,d). \tag{58}$$

If $d > \tilde{d}(h_z)$, there is one real eigenvalue $\sqrt{\kappa_1} > 0$; otherwise there are no nonzero real eigenvalues. Hence, the oscillatory component $\mathscr{G}^{(1)}$ is present only if $d > \tilde{d}(h_z)$. In passing, we note that the function $\tilde{d}(h_z)$ has the property $\lim_{h \to 0} \tilde{d}(h) = 1$. Introducing $\sqrt{\kappa_p} = i\sqrt{\nu_p}$ yields an infinite number of eigenvalues $0 < \sqrt{\nu_2} < \sqrt{\nu_3} < \cdots$. However, we only consider the $M^C - 2$ smallest because every eigenvector $\mathscr{H}^{(q)}$, $q > M^C - 1$, is a linear combination of $\mathscr{H}^{(0)}, \mathscr{H}^{(1)}, \ldots, \mathscr{H}^{(M^C-1)}$.

The eigenvalues $\sqrt{\kappa_1}$ and $\sqrt{\nu_p}$ are related to $\sqrt{\lambda_1}$ and $\sqrt{\lambda_p} = i\sqrt{\mu_p}$ through

$$\frac{2}{h_z^2}(\cosh(\sqrt{\kappa}\,h_z) - 1) = \frac{2}{h_x^2}(1 - \cos(\sqrt{\lambda}\,h_x)). \tag{59}$$

We only consider $\sqrt{\lambda_1} > 0$ and $\sqrt{\mu_p} > 0$; a negative value only interchanges the meaning of A_p and B_p in Eqs. (56), (57).

We define the scalar product and norm for grid functions f, g as

$$\langle f, g \rangle_h = \sum_{j=2}^{M^C} \tilde{f}_j g_j, \quad \|f\|_h^2 = \langle f, f \rangle_h. \tag{60}$$

It is shown in [10] that

$$\langle D_-^z \mathscr{H}^{(p)}, D_-^z \mathscr{H}^{(q)} \rangle_h = 0, \qquad \text{for} \quad p \neq q. \tag{61}$$

To find the value of the functions $\mathscr{G}^{(p)}$, $p \geqslant 1$, we use the orthogonality of the eigenvectors

$$\mathscr{G}_j^{(p)} = \frac{\langle D_-^z \phi(x_j, \cdot), D_-^z \mathscr{H}^{(p)} \rangle_h}{\|D_-^z \mathscr{H}^{(p)}\|_h^2}, \quad p = 1, 2, \ldots, M^C - 1. \tag{62}$$

Similarly to the continuous case, the eigenvactor $\mathscr{H}^{(0)}$ is annihilated by D_-^z. Instead, its coefficient is found by

$$\mathscr{G}_k^{(0)} = \phi(x_k, z_j) - \sum_{p=1}^{M^C-1} \frac{\langle D_-^z \phi(x_k, \cdot), D_-^z \mathscr{H}^{(p)} \rangle_h}{\|D_-^z \mathscr{H}^{(p)}\|_h^2} \mathscr{H}^{(p)}(z_j). \tag{63}$$

To obtain a bounded solution, there must be no linearly growing modes ahead of or behind the body: $B_0 = 0$. This is imposed by

$$D_0^x \phi(x_k, z_1) - \sum_{p=1}^{M^C-1} \frac{\langle D_0^x D_-^z \phi(x_k, \cdot), D_-^z \mathscr{H}^{(p)} \rangle_h}{\|D_-^z \mathscr{H}^{(p)}\|_h^2} \times \mathscr{H}^{(p)}(z_1) = 0. \tag{64}$$

Furthermore, there can only be exponentially decaying modes; $A_p = 0$ ahead of the body and $B_p = 0$ behind it for $p = 2, 3, \ldots, M^C - 1$. This implies $D_0^x \mathscr{G}_1^{(p)} = \mathscr{G}_1^{(p)} \sinh \sqrt{\mu_p}\,h_x/h_x$ and $D_0^x \mathscr{G}_{N^C}^{(p)} = -\mathscr{G}_{N^C}^{(p)} \sinh \sqrt{\mu_p}\,h_x/h_x$. Hence, combining the above relations yields

$$\langle D_0^x D_-^z \phi(x_1, \cdot), D_-^z \mathscr{H}^{(p)} \rangle_h - \frac{\sinh \sqrt{\mu_p}\,h_x}{h_x} \langle D_-^z \phi(x_1, \cdot), D_-^z \mathscr{H}^{(p)} \rangle_h = 0 \tag{65}$$

$$\langle D_0^x D_-^z \phi(x_{N^C}, \cdot), D_-^z \mathscr{H}^{(p)} \rangle_h + \frac{\sinh \sqrt{\mu_p}\,h_x}{h_x} \langle D_-^z \phi(x_{N^C}, \cdot), D_-^z \mathscr{H}^{(p)} \rangle_h = 0. \tag{66}$$

Similar to the continuous case, the upstream condition, Eq. (5), implies

$$\langle D_-^z \phi(x_1, \cdot), D_-^z \mathscr{H}^{(1)} \rangle_h = 0 \tag{67}$$

$$\langle D_0^x D_-^z \phi(x_1, \cdot), D_-^z \mathscr{H}^{(1)} \rangle_h = 0. \tag{68}$$

As in the continuous case, a constant function is the solution of the homogeneous discrete counterpart of Eqs. (1)–(5) and the in and outflow boundary conditions Eqs. (64)–(68). To obtain a non-singular problem, this constant is fixed by replacing the condition $B_0 = 0$ ahead of the body by $\mathscr{G}_1^{(0)} = 0$. This is imposed by applying Eq. (63) for $k = 1, j = 1$.

In contrast to the continuous case, it is not possible to guarantee $B_0 = 0$ ahead of the body. That is, the difference

scheme is not conservative. Two main sources for non-conservation can be distinguished in our scheme. First, the interpolation between the grid functions is not conservative and, second, the difference equation on the curvilinear grid is not written in conservative form. However, conservation is not crucial as long as the solution is smooth on the grid. The size of B_0 ahead of the body is therefore only considered as a measure of the accuracy of the solution.

To summarize, we have M^C+1 boundary conditions at $x=a$ and M^C-1 at $x=b$. At the boundary $x=a$, we enforce the linear relations Eqs. (63), (65), (67), (68) between the grid function $\phi_{k,j}$ at $j=1, 2, ..., M^C$ and $k=0, 1, 2$. At $x=b$, we impose the linear relations Eqs. (64), (66). They couple the grid function at the grid points (x_j, z_k), where $k=N^C-1$, N^C, N^C+1 and $j=1, 2, ..., M^C$.

6. THE REMAINING BOUNDARY CONDITIONS

To discretize the boundary condition on the body, we transform Eq. (4) to the (r, s) plane according to

$$\frac{z_r^2+x_r^2}{\det(J)}\frac{\partial\phi}{\partial s}-\frac{z_r z_s+x_r x_s}{\det(J)}\frac{\partial\phi}{\partial r}-z_r=0, \tag{69}$$

where $\det(J)=x_r z_s-z_r x_s$. Now, $\partial/\partial r$ is discretized by a central difference and $\partial/\partial s$ by the second-order accurate one-sided formula:

$$\frac{\partial\phi}{\partial s}(r_j, s_1)=\frac{1}{2h_s}(-\phi_{j,3}+4\phi_{j,2}-3\phi_{j,1})+O(h_s^2). \tag{70}$$

The periodic boundary condition on grid G_B yields $\phi_{j,k}\equiv\phi_{j+N^B-1,k}$. This defines Eq. (21) at the grid lines r_1 and r_{N^B-1}.

We discretize the z-derivative in the boundary condition at the free surface z_{M^C} by a central difference. This formula contains the grid function at the grid line z_{M^C+1}, which is outside the grid. It is eliminated by also enforcing the discrete Laplace operator at the grid line z_{M^C}. This yields

$$(\phi_{xx}+\phi_{zz})(x_j, z_{M^C})=\left(\left(1-\frac{h_z}{2}\right)D_+^x D_-^x+D_-^z\right)\phi_{j,M^C}+\mathcal{O}(h_z^2)+\mathcal{O}(h_x^2). \tag{71}$$

Similarly, the boundary condition at the bottom is discretized by

$$\phi_z(x_j, z_1)=\left(D_+^z+\frac{h_z}{2}D_+^x D_-^x\right)\phi_{j,1}+\mathcal{O}(h_z^2)+\mathcal{O}(h_z h_x^2). \tag{72}$$

7. THE INTERPOLATION RELATIONS

The grid functions on the component grids are coupled by interpolation relations. They are imposed at the grid points on the grid line s_{M^B} on the grid G_B and at the used grid points which are neighbors to unused grid points on the grid G_C, cf. Fig. 4. In the following, they will be called the interpolating grid points. Our difference scheme is a second-order accurate approximation to a second-order equation and the component grids have an overlap which is proportional to the grid size. To obtain the same order of accuracy for the total solution, it is necessary to use (at least) third-order accurate interpolation, cf. [2]. For example, let (x_n, z_m) be a interpolating grid point on the grid G_C and let $\tilde r, \tilde s$ satisfy $x_n=x^B(\tilde r, \tilde s)$ and $z_m=z^B(\tilde r, \tilde s)$. Let ϕ^C be the grid function on the grid G_C and ϕ^B the grid function on the grid G_B. The biquadratic interpolation yields the linear relation

$$\phi_{n,m}^C-\sum_{p=-1}^{1}\sum_{l=-1}^{1}\alpha_p(\tilde r)\,\beta_l(\tilde s)\,\phi_{j+p,k+l}^B=0, \tag{73}$$

where

$$\begin{aligned}
\alpha_{-1}(\tilde r)&=\Delta r_j\,\Delta r_{j+1}/2h_r^2, & \beta_{-1}(\tilde s)&=\Delta s_k\,\Delta s_{k+1}/2h_s^2\\
\alpha_0(\tilde r)&=-\Delta r_{j-1}\,\Delta r_{j+1}/h_r^2, & \beta_0(\tilde s)&=-\Delta s_{k-1}\,\Delta s_{k+1}/h_s^2\\
\alpha_1(\tilde r)&=\Delta r_{j-1}\,\Delta r_j/2h_r^2, & \beta_1(\tilde s)&=\Delta s_{k-1}\,\Delta s_k/2h_s^2
\end{aligned} \tag{74}$$

with $\Delta r_q=\tilde r-r_q$ and $\Delta s_q=\tilde s-s_q$, $q=j-1, j, j+1$. Here, $r_{j-1}\leqslant\tilde r\leqslant r_{j+1}$ and $s_{k-1}\leqslant\tilde s\leqslant s_{k+1}$. In practice, the mapping functions x^B and z^B are often only known at the grid points in G_B. In that case, $\tilde r$ and $\tilde s$ must be interpolated from the values at the grid points. In order to obtain third-order accuracy in Eq. (73) it is also necessary to use third-order interpolation when $\tilde r$ and $\tilde s$ are calculated.

The interpolating grid points on the grid G_B yield similar linear relations between the grid functions. However, the grid G_C is Cartesian so $\tilde r$ and $\tilde s$ can be found analytically. This closes the system. We now have the same number of equations as used grid points.

8. SOLVING THE LINEAR SYSTEM OF EQUATIONS

The sparse linear system of equations was solved by LU-decomposition followed by iterative improvement until the norm of the residual did not decrese further. We used the HARWELL sparse matrix package. In this package the pivoting strategy can be biased continuously between numeric and sparsity concerns. It was found necessary to bias the pivoting towards numeric concern when the number of equations exceeded ≈ 2000. Otherwise, the resulting LU-decomposition became so poor that the iterative

improvement diverged. All calculations presented in the subsequent sections were performed in 32 bits precision on a Sun SPARC station SLC.

9. VALIDATING THE DIFFERENCE SCHEME

The following test was designed to check the order of accuracy of the difference scheme. A solution is chosen for the continuous problem, which need not satisfy the differential equation or the boundary conditions. The differential equation and the boundary conditions are applied to the solution to obtain a continuous forcing function. The forcing function for the discrete problem is taken to be the continuous forcing at the grid points. The order of accuracy is then found by studying the difference between the discrete solution and the continuous solution at the grid points for different grid sizes. At the inflow and outflow boundaries the continuous problem satisfies an infinite number of relations, but it is only possible to enforce a finite number of relations for the discrete problem. There is no obvious restriction of the relations for the continuous problem to the discrete problem, and for this reason the discrete relations are simply applied to the continuous solution to obtain the forcing for each discrete relation. The behavior of these relations are instead investigated separately; this is described below.

A circular cylinder of radius R was used as test body. The non-dimensional depth was $d = 5R = 7.8125$ and the distance between the surface and the center of the cylinder was $2R$. The radius of the outer boundary of the grid around the cylinder was $1.5R$ and the computational domain was between $-2.7 \leqslant x \leqslant 2.7$. This size corresponds to three grid lines in the coarsest Cartesian grid ahead of and behind the grid around the cylinder. The coarsest composite grid is shown in Fig. 5. The test was applied for the function

$$u(x, z) = \alpha(x^4 + (z + d/2)^4), \tag{75}$$

where α was chosen to make $\max u = 1$ in the computational domain. The difference between the exact and the discrete solutions as functions of the grid size is given in Table I. The result on the finest grid suggests that that solution was affected by roundoff errors. Otherwise, the test confirms that our difference scheme is second-order accurate when the discrete inflow and outflow boundary conditions are satisfied exactly.

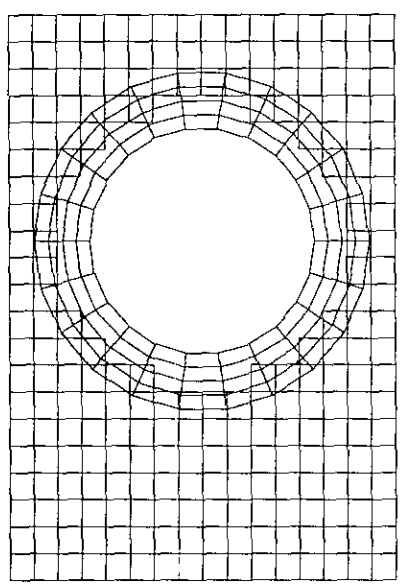

FIG. 5. The coarsest composite grid around the test body.

TABLE I

The Difference $u - u_h$ Measured in Maximum Norm at the Grid Points

Grid size	N_B	M_B	N_C	M_C	$\|u - u_h\|_\infty$
$4h$	24	5	17	22	7.80×10^{-2}
$2h$	47	9	33	43	1.69×10^{-2}
$4h/3$	70	13	49	64	7.12×10^{-3}
h	93	17	65	85	4.42×10^{-3}

The subsequent experiment was done to investigate the quality of the boundary conditions at $x = a$ and $x = b$. Two solutions, ϕ_1 and ϕ_2, were computed around the test body. The computational domains in the x-direction were $a_1 < x < b_1$ and $a_2 < x < b_2$, respectively, where $a_1 \ll a_2$ and $b_2 \ll b_1$. After the solution in $a_2 < x < b_2$ had been calculated, it was extended to $a_1 < x < b_1$ by the eigenvector expansion given by Eq. (51). To make it easier to compare the two solutions, a constant was added to each of them such that $\phi_j(a_1, 0) = 0$. The shorter of the grids was identical to the grid in Table I with grid size $2h$. The longer grid was identical to the shorter grid in $a_2 \leqslant x \leqslant b_2$, but the Cartesian component grid was extended to $a_1 \leqslant x < a_2$ and $b_2 < x \leqslant b_1$ by increasing N_C and keeping h_x unchanged. The difference, $\phi_1 - \phi_2$, measured in maximum norm over $a_1 < x < b_1$ is given in Table II and the conclusion is that the difference is negligible. Obviously, there is a considerable gain in decreasing $b - a$; the number of equations decreases and the solution close to the body becomes less sensitive to roundoff errors, since the eigenvalue of smallest magnitude of the discrete operator behaves like $(b - a)^{-2}$, cf. [10].

To further validate the scheme, the lift and drag coef-

TABLE II

Extension of the Solution by the Eigenvector Expansion

a_1	b_1	a_2	b_2	$\|\phi_1 - \phi_2\|_\infty$	$\|\phi_1\|_\infty$
-5.4	5.4	-2.7	2.7	9.47×10^{-6}	5.31

TABLE III

The Lift and Drag Coefficients and the Conservation Error for the Circular Cylinder

C_L	C_D	B_0 ahead	N_B	M_B	N_C	M_C
2.0770	1.1323	5.74×10^{-3}	24	5	17	22
2.0586	1.1979	1.81×10^{-4}	47	9	33	43
2.0583	1.1970	-2.45×10^{-4}	70	13	49	64
2.0574	1.1963	4.66×10^{-5}	93	17	65	85

ficients and the surface elevation for a circular cylinder were compared with those reported in [5]. They used a boundary integral method with a kernel that satisfied the boundary condition on the free surface and the upstream condition. The finite depth was modeled by inserting a horizontal plate of length $80R$ at the depth $5R$, where R is the radius of the cylinder. Outside that region the depth was infinite. The cylinder had its center submerged $2R$ below the surface and the non-dimensional depth was $d = 5R = 7.8125$, which corresponds to the Froude number $F_d = U/\sqrt{gD} = 1/\sqrt{d} = 0.3578$. Here, U is the speed of the body, g is the acceleration of gravity, and D is the depth of the liquid. In our computation, the same grids were used as for the above-described test of the accuracy. The lift and drag coefficients were found by integrating the pressure given by the Bernoulli equation. Expressed in our scaled variables, this yielded

$$C_L = \frac{1}{R}\oint_{\Gamma_B} (2\phi_x + \phi_x^2 + \phi_z^2)\, dx$$

$$C_D = \frac{1}{R}\oint_{\Gamma_B} (2\phi_x + \phi_x^2 + \phi_z^2)\, dz. \tag{76}$$

The result is given in Table III, where also the conservation error, B_0 ahead of the body, is reported. The oscillatory behavior of B_0 indicates that roundoff errors affected the solutions on the two finer grids. The results reported in [5] were $C_L = 2.04$ and $C_D = 1.19$.

It is consistent with the linearized free surface boundary condition Eq. (2) to approximate the elevation of the free surface by $\eta(x) = -\phi_x(x, 0)$. The elevation reported in [5], together with the present results are given in Fig. 6. In our calculation, the surface elevation computed on the three finest grids was identical within graphical accuracy. Only a qualitative comparison with the results in [5] is possible, because of the difficulty to accurately duplicate Fig. 12 in that paper. However, within graphical accuracy, both the phase and the amplitude of the surface elevation agree well.

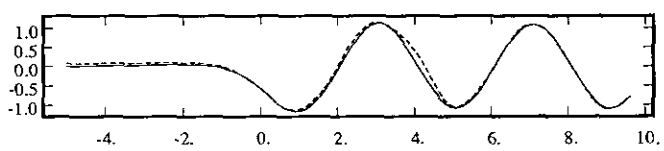

FIG. 6. The elevation of the surface above the test body. The solid line corresponds to the present calculation on the finest grid. The dashed line represents the result reported in [5].

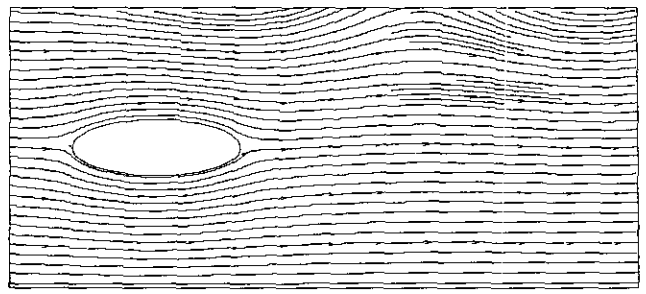

FIG. 7. Streamlines around the ellipse of length 3.0.

10. NUMERICAL EXAMPLES

To exemplify the use of the present method, we studied how the flow about ellipses and rounded rectangles depend on the length of the body at a fixed Froude number. In particular, we calculated the lift and drag coefficients. In all computations, the non-dimensional depth was fixed to $d = 5$ which yielded a Froude number $F_d = 1/\sqrt{5}$.

The ellipses had the horizontal semiaxis submerged $0.5d$ below the surface and the length of the vertical semiaxis was $0.1d$. The outer boundary of the grid around the ellipse was chosen to be an ellipse which semiaxes were $0.15d$ larger than the corresponding semiaxes of the body. To obtain reasonably accurate solutions, the grid sizes were chosen to approximately equal those of grid size $2h$ in the aforementioned accuracy test, cf. Table I. The lift and drag coefficients were defined as in Eq. (76) except that we replaced R by the length of the horizontal semiaxis. To exemplify the

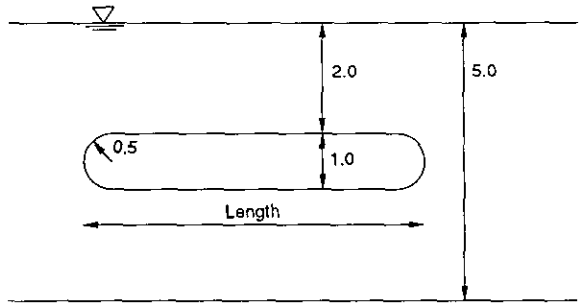

FIG. 8. The geometry of the rounded rectangle.

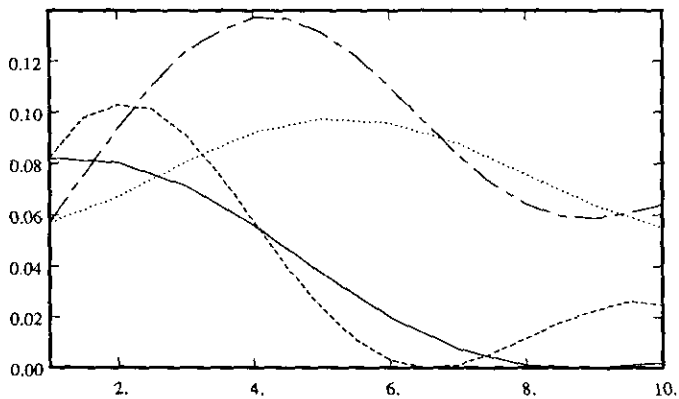

FIG. 9. Lift and drag coefficient as functions of the length of the ellipse and the rounded rectangle. The solid line represents C_D for the ellipse, the dashed line is C_D for the rounded rectangle, the dotted line corresponds to C_L for the ellipse, and the long-short dashed line represents C_L for the rounded rectangle.

flow field, we present the streamlines around the ellipse of length 3.0 in Fig. 7.

The thickness of the rounded rectangle was set to $0.2d$, the radius of the rounded ends to $0.1d$, and the upper horizontal boundary was submerged $0.4d$ below the surface, cf. Fig. 8. The outer boundary of the grid was chosen to be the rounded rectangle situated $0.15d$ outside the body. The grid sizes were chosen by the same rule as for the grid around the ellipse. For this geometry we replaced R in Eq. (76) by half the length of the body. The results are given in Fig. 9. For both the ellipse and the rounded rectangle, we found that the waves generated by the front and the aft part of the body cancel each other at certain lengths, resulting in a minimum in C_D. The minima occur for different values of the length for the two geometries which implies that the more slenderly shaped ellipse does not always generate less drag compared to the rounded rectangle of the same length. We remark that C_D only includes the wave drag. The total drag, which also contains viscous drag, is likely to be larger for the rounded rectangle than for the ellipse.

ACKNOWLEDGMENTS

Professor H.-O. Kreiss is greatly acknowledged for many fruitful discussions on the present problem. Thanks also to Drs. W. D. Henshaw, G. Chesshire, and D. L. Brown for valuable guidance on the use of composite grids. This work was partially supprted by U.S. Navy Contract N-00014-90-J-1382 and by the U.S. Department of Energy through Los Alamos National Laboratory.

REFERENCES

1. D. L. Brown, G. Chesshire, and W. D. Henshaw, LA-UR-90-3729, Los Alamos National Laboratory, Los Alamos, NM (unpublished).
2. G. Chesshire and W. D. Henshaw, *J. Comput. Phys.* **90**, 1 (1990).
3. C. W. Dawson, in *Proceedings, Second International Conference on Numerical Ship Hydrodynamics, Berkeley, 1977*, p. 30.
4. L. J. Doctors and R. F. Beck, *J. Ship Res.* **31**, 227 (1987).
5. J. P. Giesing and A. M. O. Smith, *J. Fluid Mech.* **28**, 113 (1967).
6. P. S. Jensen, *J. Ship Res.* **31**, 14 (1987).
7. Y. H. Kim and T. R. Lucas, in *Proceedings, 18th Symposium on Naval Hydrodynamics, Ann Arbor, Michigan, 1990.*
8. J. F. Malmliden and N. A. Petersson, CAM-report 92-14, Dept. of Mathematics, University of California, Los Angeles, CA (unpublished).
9. C. C. Mei and H. S. Chen, *Int. J. Numer. Methods Eng.* **10**, 1153 (1976).
10. N. A. Petersson, Ph.D. thesis, Dept. of Numerical Analysis and Computing Science, Royal Institute of Technology, TRITA-NA-9001, 1990 (unpublished).
11. J. F. Thompson, Z. U. A. Warsi, and C. W. Mastin, *Numerical Grid Generation* (North-Holland, Amsterdam, 1985), p. 126.
12. J. V. Wehausen and E. V. Laitone, "Surface Waves," in *Encyclopedia of Physics, vol. IX*, edited by S. Flügge (Springer-Verlag, New York/Berlin, 1960), p. 470.